Conversion of Flexible Spin Crossover Metal–Organic Frameworks Macrocrystals to Nanocrystals Using Ultrasound Energy: A Study on Structural Integrity by MicroED and Charge-Transport Properties

A. Martinez-Martinez, S. Gullace, E. Resines-Urien, L. Martín-Pérez, J. Collado, R. Arranz, E. Burzurí, C. Santiago, E. C. Sañudo, J. Sanchez Costa

This is the peer reviewed version of the following article: A. Martinez-Martinez, S. Gullace, E. Resines-Urien, L. Martín-Pérez, J. Collado, R. Arranz, E. Burzurí, C. Santiago, E. C. Sañudo, J. Sanchez Costa, Conversion of Flexible Spin Crossover Metal–Organic Frameworks Macrocrystals to Nanocrystals Using Ultrasound Energy: A Study on Structural Integrity by MicroED and Charge-Transport Properties. Small 2024, 2408966, which has been published in final form at https://onlinelibrary.wiley.com/doi/10.1002/smll.202408966 This article may be used for non-commercial purposes in accordance with Wiley Terms and Conditions for Use of Self-Archived Versions. This article may not be enhanced, enriched or otherwise transformed into a derivative work, without express permission from Wiley or by statutory rights under applicable legislation. Copyright notices must not be removed, obscured or modified. The article must be linked to Wiley's version of record on Wiley Online Library and any embedding, framing or otherwise making available the article or pages thereof by third parties from platforms, services and websites other than Wiley Online Library must be prohibited.

To cite this version

A. Martinez-Martinez, S. Gullace, E. Resines-Urien, L. Martín-Pérez, J. Collado, R. Arranz, E. Burzurí, C. Santiago, E. C. Sañudo, J. Sanchez Costa, Conversion of Flexible Spin Crossover Metal–Organic Frameworks Macrocrystals to Nanocrystals Using Ultrasound Energy: A Study on Structural Integrity by MicroED and Charge-Transport Properties (2024). https://hdl.handle.net/20.500.12614/3915

Licensing

This article may be used for noncommercial purposes in accordance with Wiley Terms and Conditions for Use of Self-Archived Versions https://authorservices.wiley.com/author-resources/Journal-Authors/licensing/self-archiving.html (last accessed July 2023). Copyright Wiley-VCH Verlag GmbH & Co. KGaA.

Embargo

This version (post-print or accepted manuscript) of the article has been deposited in the Institutional Repository of IMDEA Nanociencia with access rights embargoed until 26.12.2025.

Conversion of Flexible Spin Crossover Metal-Organic Frameworks Macrocrystals to Nanocrystals using Ultrasound Energy: A MicroED Analysis of Structural Transformations

Ana Martinez-Martinez,[a] Sara Gullace,[a] Esther Resines-Urien,[a] Lucia Martín-Pérez,[a] Javier Collado,[b] Rocío Arranz,[b] Enrique Burzurí,[a,c,d] César Santiago,[b] E. Carolina Sañudo[e*] and José Sanchez Costa[a*]

[a]*IMDEA Nanociencia, C/ Faraday 9, Ciudad Universitaria de Cantoblanco, 28049 Madrid, Spain*
[b]*Department of Macromolecular Structure, National Centre for Biotechnology (CNB-CSIC), 28049, Madrid, Spain*
[c]*Departamento de Física de La Materia Condensada, Universidad Autónoma de Madrid, Madrid, 28049, Spain*
[d]*Condensed Matter Physics Center (IFIMAC) and Instituto Universitario de Ciencia de Materiales "Nicolás Cabrera" (INC), Universidad Autónoma de Madrid, Madrid, 28049, Spain*
[e]*Departament de Química Inorgànica i Orgànica, Secció de Química Inorgànica, Universidad de Barcelona, C/Martí i Franqués 1-11, 08028 Barcelona, Spain*

Keywords: Metal-organic frameworks, spin crossover, nanostructuration, charge transport, microelectron diffraction

ABSTRACT

Metal-Organic Frameworks (MOFs) attract attention for their intrinsic porosity, large surface area, and functional versatility. To fully utilize their potential in applications requiring precise control at smaller scales, it is essential to overcome challenges associated with their bulk form. This is particularly difficult for 3D MOFs with spin crossover (SCO) behavior, which undergo a reversible transition between high-spin and low-spin states in response to external stimuli. Maintaining their structural integrity and SCO properties at the nanoscale remains a significant challenge, yet these properties make them ideal candidates for sensors, data storage, and molecular switch applications. This study reports the synthesis of nanocrystals of the well-known SCO MOF $[Fe_2(H_{0.67}bdt)_3]\cdot xH_2O$ (**1**, x = 0-10, bdt^{2-} = 1,4-benzeneditetrazolate), which exhibits both magnetic and charge transport properties. The nanocrystals are obtained through sonication of macrocrystals, and the preservation of their crystalline structure at the nanoscale is explored using Microcrystal Electron Diffraction (MicroED). A comparison between macro- and nanocrystals highlights the structural integrity, underlining the potential for further miniaturization of MOFs for advanced technological applications.

1. Introduction

Metal-organic frameworks (MOFs) have become captivating materials with unlimited potential in multitude applications, owing to their customizable porosity, large surface area and functional versatility.[1,2] However, to maximize their utility, it is often necessary to overcome the challenges associated with their bulk form, particularly in applications[3] that require precise control and integration at smaller scales.

Miniaturization of MOFs, especially those with switchable spin crossover behavior (SCO),[4,5] holds great promise for improving their functionality and applicability in various fields.[6,7] (RSC Advances, 2014, 4, 34760) MOFs with SCO[8] undergo a reversible transition between high- and low-spin (HS and LS) states in response to external stimuli, making them promising candidates for sensing,[9,10] data storage,[11,12] energy saving[13] and molecular switch applications.[14,15]

However, their technological application has not been successfully implemented, as it remains challenging to maintain their properties at the nanoscale.[16,17] Therefore, exploring and exploiting SCO phenomena in this size regime requires innovative approaches to preserve structural integrity and physico-chemical properties,[18] whilst taking advantage of the unique properties conferred by miniaturization.[19]

Nanostructuring of MOFs for integration in devices can be accomplished in two different manners:[20] direct synthesis onto surfaces or pre-formation of the material to be subsequently deposited on the device. Direct synthesis requires both the MOF precursors and the surface or device on which they are to be deposited to share a reaction media,[21–23] which in many instances represents a problem as the synthesis conditions for MOFs often involve high temperatures and damaging solvents. In addition, the synthesis of surface-mounted MOFs requires the optimization of several subsequent steps of the formation of self-assembled monolayers of metal precursor and organic ligand, as well as surface functionalization to optimize morphology, crystallite orientation, surface roughness and surface coverage.[24,25] Therefore, an effective alternative is to pre-form the material prior to its deposition on the required surface.

Deposition of pre-formed materials typically involves two primary steps. Initially, the desired material is synthesized, either as a colloidal dispersion (employing a bottom-up approach)[26–28] or as a bulk material, which can then be suspended or undergo physical or liquid-phase delamination (a top-down approach).[29–32] In the subsequent step, the material is deposited on the desired surface. Bottom-up deposition involves preparing MOF particles with precise sizes and then transferring them onto substrates, e.g. through dip-coating.[33] However, the synthesis of nanosized MOFs involves the adjustment of parameters such as precursors concentration, time, temperature, and energy source to limit the crystal growth.[34,35] Alternatively, in top-down deposition, that has been widely used to obtain nanosheets from 2D MOFs,[36] the material is exfoliated in liquid phase, often requiring sonication assistance to achieve delamination into an easily processable suspension. Nevertheless, sonication in 3D MOFs has been reported to lead to the reduction of sizes from micro to a few hundred nanometres.[30]

Nanocrystals exhibit unique characteristics due to their reduced dimensions, the interpretation of which requires precise knowledge of their atomic arrangement. Therefore, understanding their crystalline structure is crucial for tailoring their properties to specific applications. Microcrystal Electron Diffraction (MicroED)[37] emerges as a revolutionary solution, offering unparalleled insights into nanocrystal structures at the atomic level. Utilizing Microelectron diffraction, MicroED provides high-resolution data, enabling the identification of bond lengths, angles, and defects[38,39] at the sub microscale crystals.[40] Moreover, its ability to analyze nanocrystals[41] *in-situ* without extensive sample preparation makes it invaluable for real-time observations of dynamic processes. Overall, MicroED plays a pivotal role in advancing nanoscience and nanotechnology by facilitating the design of nanocrystals with tailored properties and enhanced functionalities.[42,43]

Herein, the obtention of nanocrystals of the well-documented MOF $[Fe_2(H_{0.67}bdt)_3]\cdot xH_2O$ (**1**) (x = 0-10 H_2O, bdt^{2-}= 1,4-benzeneditetrazolate) is reported. This compound consists of Fe(II) metal centers octahedrally coordinated to H_2bdt ligands. The interest of this compound lies mainly in the coexistence of the spin crossover magnetic properties and charge transport properties.[44] Hitherto, this compound has been investigated in the form of single crystal in several studies.[45,46] Here, the exhaustive comparison between the macrocrystals (**1**) and the nanocrystals (**1_{nano}**) obtained by sonication of the former is presented. In addition, using the MicroED technique, the preservation of the crystalline structure in the nanoscale regime is demonstrated, validating the applicability of this approach for structural characterization of miniaturized MOFs.

2. Results and Discussion

2.1. Morphological characterization: Scanning Electron Microscopy (SEM) and Atomic Force Microscopy (AFM)

1_{nano} was obtained by sonication of **1** macrocrystals in isopropanol, as described in **Section 2.6** and **Figure S1**. Morphological characterization was performed by microscopic techniques to confirm the successful formation of nanocrystals. SEM micrographs were obtained for both **1** and **1_{nano}** to enable a precise comparison. As previously documented,[44,45] **1** adopts a hexagonal polyhedral morphology. The hexagonal face of the polyhedron corresponding to the *ab* plane of the crystal structure is shown in **Figure 1a**, with an average side length of approximately 95 μm and a diagonal of around 186 μm. The rectangular lateral face associated with the *ac* plane is visible in **Figure 1b**, measuring about 214 μm in length (refer to **Figures S2†** and **S3†** for further details). Concerning the nanocrystals, **Figure 1c** presents a SEM image of $\mathbf{1_{nano}}$ positioned between gold electrodes by dielectrophoresis (DEP) for subsequent electrical characterization (see **Section 2.4**). DEP is a technique well-suited for accurately placing nanomaterials onto devices.[47–49] A solution containing dispersed $\mathbf{1_{nano}}$ in isopropanol (1 mg/mL) is drop-casted onto the devices, while simultaneously applying a sinusoidal AC voltage between the electrodes to create a non-uniform electric field. This electric field attracts and aligns the nanocrystals to regions with significant field gradients, specifically the gaps between the electrodes. Excess solvent is removed from the substrate with a gentle nitrogen stream.

The nanocrystals display irregular geometries and are significantly smaller than the macroscale structures (additional images are provided in **Figure S4†**). To further investigate the size, particularly the height of the nanocrystals, AFM was employed. **Figure 1d** and **1e** show the AFM height map of the nanocrystals deposited *via* dielectrophoresis between interdigitated gold electrodes, alongside the respective height profile. The lateral dimension of the nanocrystals ranges between 1-1.5 μm and the height between 90-100 nm. For a more extensive and comprehensive analysis of the height of the nanocrystals, a statistical analysis was carried out in a large amount of nanocrystals deposited by drop-casting on a Si/SiO_2 substrate, as shown in **Figure 1f.** The thickness distribution follows a decreasing exponential behavior, with about 83% of the nanocrystals being smaller than 100 nm in height, confirming their nanometric size (additional measurements are shown in **Figure S5†** and **S6†**).

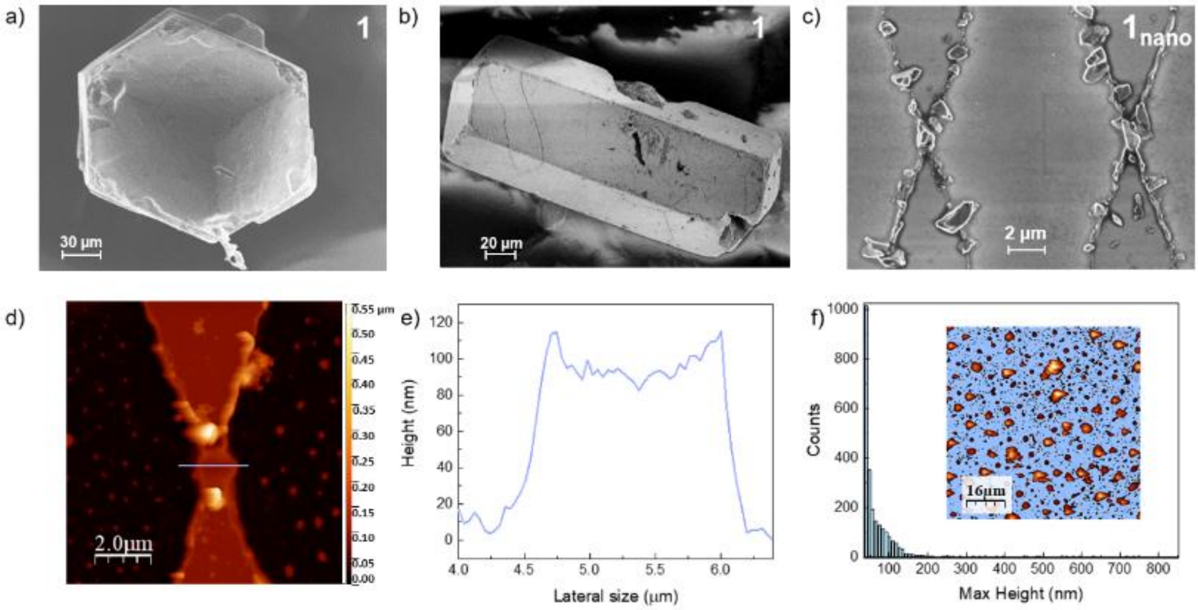

Figure 1. a) SEM image of the hexagonal face of **1**. b) SEM image of the rectangular face of **1** c) SEM image of $\mathbf{1_{nano}}$ dielectrophoretically placed between interdigitated gold electrodes. d) AFM topographic characterization of $\mathbf{1_{nano}}$ between gold electrodes. e) Height profile of the nanocrystals shown in (d). f) $\mathbf{1_{nano}}$ thickness distribution of the nanocrystals shown in the inset.

2.2. Structural Resolution: A MicroED analysis

The nanometric size of $\mathbf{1_{nano}}$ impedes the resolution of the crystalline structure by conventional SCXRD, therefore, the structure determination was conducted using the MicroED technique with continuous rotation electron diffraction (cRED) collection performed at 100 K. In this regard, 3D electron diffraction methods have demonstrated significant effectiveness in the structure determination of MOFs from nano- and micrometer-sized crystals.[37,50] Due to the strong interactions between electrons and matter, single-crystal 3D electron diffraction can be performed on nanocrystals that are significantly smaller in volume compared to those required for SCXRD.

Two TEM images of some of the nanocrystals measured using this technique are shown in **Figure 2**. The surface area size corresponds with observations from SEM and AFM. Moreover, AFM revealed that the crystal heights display a size of more than 20 nm, which is ideal for ensuring electron penetration.[51]

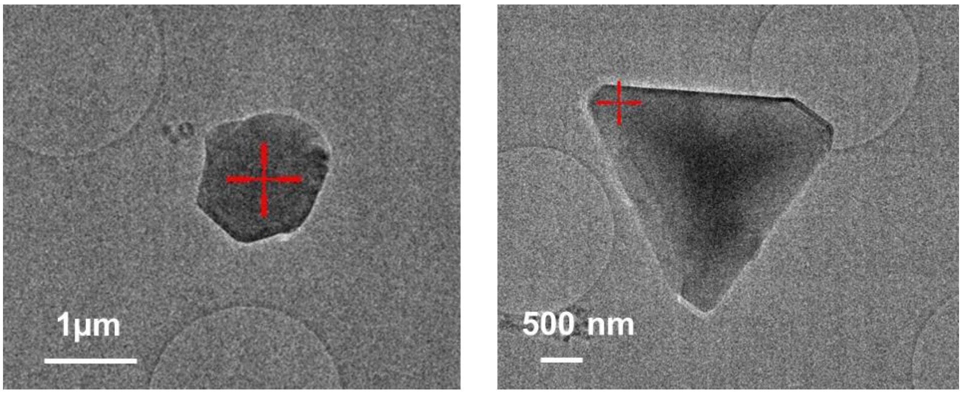

Figure 2. TEM images of two different crystals of $\mathbf{1_{nano}}$ measured by MicroED.

Unit cell parameters of $\mathbf{1_{nano}}$ were determined from one single cRED dataset to be a/b=22.53(13) Å, c = 7.33(6) Å, α/β = 90° and γ = 120°, corresponding to the trigonal crystalline system. The obtained volume of $\mathbf{1_{nano}}$ is 3227 Å^3, analogous to the volume reported for **1** at the same temperature (3206 Å^3). The asymmetric unit contains two crystallographic independent Fe(II) metal centers each coordinated to six nitrogen atoms from belonging to six different H_2bdt ligands in an octahedral geometry, defining {Fe-(tetrazolate)}$_n$ chains.

The spin state of the iron ions can be deduced by the Fe-N distances: as outlined in **Table S2†**, the Fe-N distances for **1** are found as Fe1-N: 1.945 Å and Fe2-N: 2.099 Å, corresponding with iron ions in the LS and HS state, respectively. Similarly to its bulk counterpart, the structure refinement of $\mathbf{1_{nano}}$ revealed distances (Fe1-N: 1.956 Å and Fe2-N: 2.057 Å) which are in agreement with the presence of iron centres in LS and HS states. In addition, it can be noticed in $\mathbf{1_{nano}}$ that the plane formed by the tetrazole ring of the ligand H_2bdt (maroon dotted lines in **Figure 3b**) stands out of the plane defined by the Fe centers (represented in **Figure 3** as a yellow plane) differing from this one in 6°. This results in a slight distortion of the triangular pores, where the ligands are bent inwards in one pore, and outwards in the adjacent one. Moreover, simulated powder diffractograms obtained from both structures have been compared. As can be seen in **Figure S7†**, they match perfectly, corroborating that the overall structure is preserved during the downsizing process to the nanoscale.

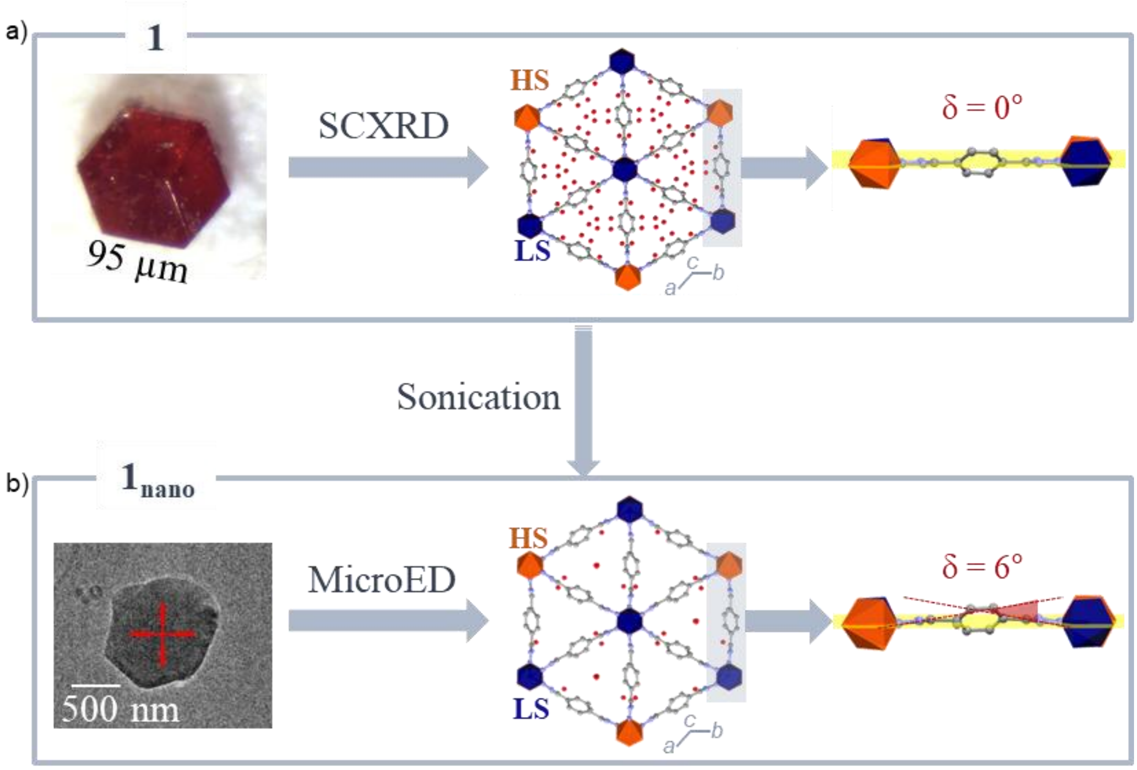

Figure 3. a) Image of **1** captured with an optical microscope along with the crystalline structure solved by SCXRD. The amplification of the H_2bdt ligand, where the tetrazole ring lies within the plane formed by the metal centers (depicted in yellow), is also shown. b) TEM image of $\mathbf{1_{nano}}$ along with its structure obtained by MicroED. The distortion of the ligand from the planar alignment is also represented. The yellow plane is the one involving the metallic centres and the dotted maroon lines are the planes involving the nitrogen atoms of the tetrazole. HS Fe(II) is shown in orange, LS Fe(II) in dark blue, C in grey, N in blue and O in red. H are omitted for clarity.

2.3. Following the spin transition *via* Raman Spectroscopy

Raman spectroscopy is a well-established tool to follow spin transition processes as it provides specific vibrational information which can be correlated to the spin state.[52–54] The main advantage of this technique is its feasibility for studies on small samples allowing focus on single crystals and micrometric samples. Raman spectroscopy was performed on crystalline samples by using a 532 nm laser, and the resulting Raman spectra were recorded between 50 and 2730 cm^{-1} range (see Figure below and further details in experimental section and S8†).

The extended Raman spectrum of **1** (**Figure S8†**, averaged over three points in the same single crystal) exhibits peaks related to the Fe-N bond stretching vibration ($\nu_{Fe\text{-}N}$) in the range 100-

500 cm^{-1} and vibrations of the H_2bdt organic ligand, *e.g.* tetrazole and phenyl ring breathing mode (ν_{rings}) centered at 1018 cm^{-1} and the C=C stretching mode ($\nu_{C=C}$) at 1626 cm^{-1}. Although the octahedral [FeN_6] unit should exhibit theoretically fifteen Raman-active modes, experimental limitations often result in the observation of fewer peaks due to silent or weak vibrational modes.[55] For this reason, the most prominent peaks observed in the Raman spectrum have been chosen affording an average $\nu_{Fe\text{-}N}$ frequency (247 cm^{-1}), as shown in **Table S3†**. Statistical analysis performed on six different crystals of **1** confirmed the reported data.

As previously mentioned, the as-synthesized material exhibits two crystallographic independent Fe(II) metal centers at room temperature, one in LS and one in HS. A fundamental characteristic of **1** is the water release-induced reverse HS to LS SCO triggered by thermal treatment.[44] The Raman study supports this observation, since the average $\nu_{Fe\text{-}N}$ undergoes a blue-shift to 294 cm^{-1} after thermal treatment (**Table S3†**), in accordance with the Fe-N bond length contraction occurring when the HS Fe(II) centers shift to the LS state.

Beyond metal–ligand stretching vibrations, the SCO in this material induced other significant alterations in the Raman spectrum, such as the red-shift of ν_{rings} and $\nu_{C=C}$. (**Figure S8** and **Table S3†**), suggesting the elongation of the bonds (single/double C-N, N-N, C-C, C=C) involved in these collective ligand vibrations. This observation implies that the ligand vibrations are directly coupled with the low-frequency Fe–N stretching modes.[56] For this reason, the ν_{rings} is chosen as the marker band to follow the Fe(II) electronic state change.

Multicomponent peak analysis evidences that four sub-bands contribute to the ν_{rings} vibration, underlining that **1** exhibits Fe centers in the HS (orange sub-bands) and LS states (blue sub-bands) in the as-synthesized material (**Figure 4a**). The HS:LS ratio can be calculated from the relative peak areas of the sub-bands (**Table S4†**). For **1** as-synthesized this ratio is 90:10 HS:LS, with the HS sub-bands more prominent than the LS ones. This predominance can be attributed to the population of the highest *d*-orbitals of the metal, which enhances the ligand-centered bands.[57] In spite of this, upon thermal dehydration, as shown in **Figure 4b**, the blue LS sub-bands become significantly more prominent in **Figure 4b** (7:93 HS:LS ratio). The peak areas for each sub-band are reported in **Table S4†**.

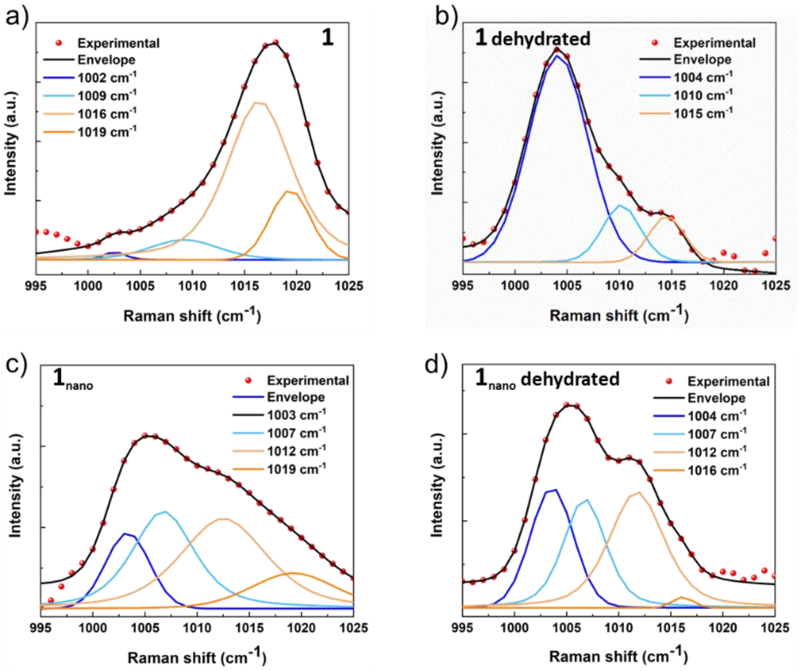

Figure 4. Multicomponent peak analysis of ν_{rings} for a) **1**, b) **1** dehydrated, c) **1$_{nano}$** and d) **1$_{nano}$** dehydrated. Orange and blue sub-bands refer to HS and LS Fe states, respectively.

Raman spectroscopy was conducted on **1$_{nano}$,** with the sample drop-casted onto filter paper to allow the study of single isolated nanocrystals. The Raman spectrum of **1$_{nano}$** closely resembles that of **1**, with $\nu_{Fe\text{-}N}$ and ν_{rings} slightly blue- and red-shifted respectively, likely due to the sonication in a non-aqueous solvent (isopropanol, see **Figure S8**, **Table S3†** and **Section 2.6** for details). Quantification of the LS sub-bands within the ν_{rings} multicomponent peak reveal a 54:46 HS:LS ratio. Consistently with the behavior of **1**, thermal dehydration of **1$_{nano}$** induced an evident reduction of the HS contribution to the ν_{rings} marker band and an alteration of the calculated HS:LS ratio to 35:65 (**Figure 4** and **Table S4†**).

Temperature-dependent Raman spectroscopy was performed on both **1** and **1$_{nano}$** . **Figure S9** shows the HS:LS ratio calculated for **1** and **1$_{nano}$** from the area of the HS and LS sub-bands used for the ν_{rings} multicomponent peak analysis at different temperatures. it was found that >90% of the Fe(HS) centers switched to the LS state at 358 K and 348 K in the case of **1** and **1$_{nano}$,** respectively. Taking into account that SCO takes place as a function of water release, the behavior is in line with different water dynamics when downsizing to the nanoscale.

Additionally, Raman spectra were acquired on **1_{nano}** immediately after its synthesis by sonication and after 9 months. The **1_{nano}** suspension in 2-propanol was stored in a closed vial in the dark. **Figure S10** shows that the ν_{rings} band did not undergo any shift, indicating that the nanocrystals suspension has long shelf-life and the spin state of the Fe centers is not altered with time.

Finally, Raman spectroscopy was conducted on **1_{nano}** after dielectrophoresis deposition in the channels between interdigitated gold electrodes on the electrical devices. The reported data are the average over 21 points collected among at least 3 different electrodic channels (see **Section 2.4** and **2.6**). While the low-frequency region of the spectra was dominated by the Si Raman peak from the substrate at 521 cm^{-1} (see **Figure S12†** for details), analysis of the ν_{rings} marker band and its sub-bands (**Table S5†)** confirmed that the nanocrystal preparation process and deposition on devices did not affect the intrinsic properties or behavior of the material.

2.4. Electrical Measurements

One of the fascinating features of **1** is the confluence of electric transport and spin transition, as previously reported.[44] In the preceding research, the investigations of the charge transport properties of this compound were carried out *via* direct contact of the tips of the probes with single-crystalline **1** in a probe station.

A rise in electrical current (*I*) with increasing temperature was observed, along with a noticeable modulation of the current corresponding to the spin transition. In particular, higher current values were observed when the system converted to a completely LS configuration, which was corroborated by Density Functional Theory (DFT) calculations.[44]

Consequently, an examination of the electrical transport in **1_{nano}** has been performed in order to evaluate whether this property is maintained after downsizing to the nanoscale. The electron transport measurements through **1_{nano}** crystals are conducted on solid-state nanoscale devices (**Figure 5a**), as explained previously.

Figure 5b shows the *IV* characteristics of **1_{nano}** at different temperatures in the range 298-428 K using a Linkam temperature controller. The measured current decreases slightly with increasing temperature until 348 K is reached. From this point onwards, it increases exponentially with temperature, as already reported for **1**. The main *IV* characteristics are roughly reproducible in all the measured devices containing **1_{nano}** (examples are shown in **Figure S14†**). The current values obtained depend on the amount of material trapped by DEP between the gold electrodes but, in most cases, it increases by at least one order of magnitude with increasing temperature up to 428 K, as in **1**. The grey line corresponds to the current measured in an empty device before carrying out DEP.

Figure 5c shows the comparison of the current increment with temperature observed at a fixed bias voltage ($V = 4$ V) for **1** and **1_{nano}**. In both cases, from about 350 K onwards, the current grows exponentially with temperature, indicative of thermally activated transport. The activation energy in this temperature region (i.e. the majority of the crystal in its LS state) significantly coincides in **1** (219 meV, see ref[44]) and in **1_{nano}** (219 meV; see **Figure S13**). This scenario contrasts with the rather different qualitative behavior observed in the low temperature region.

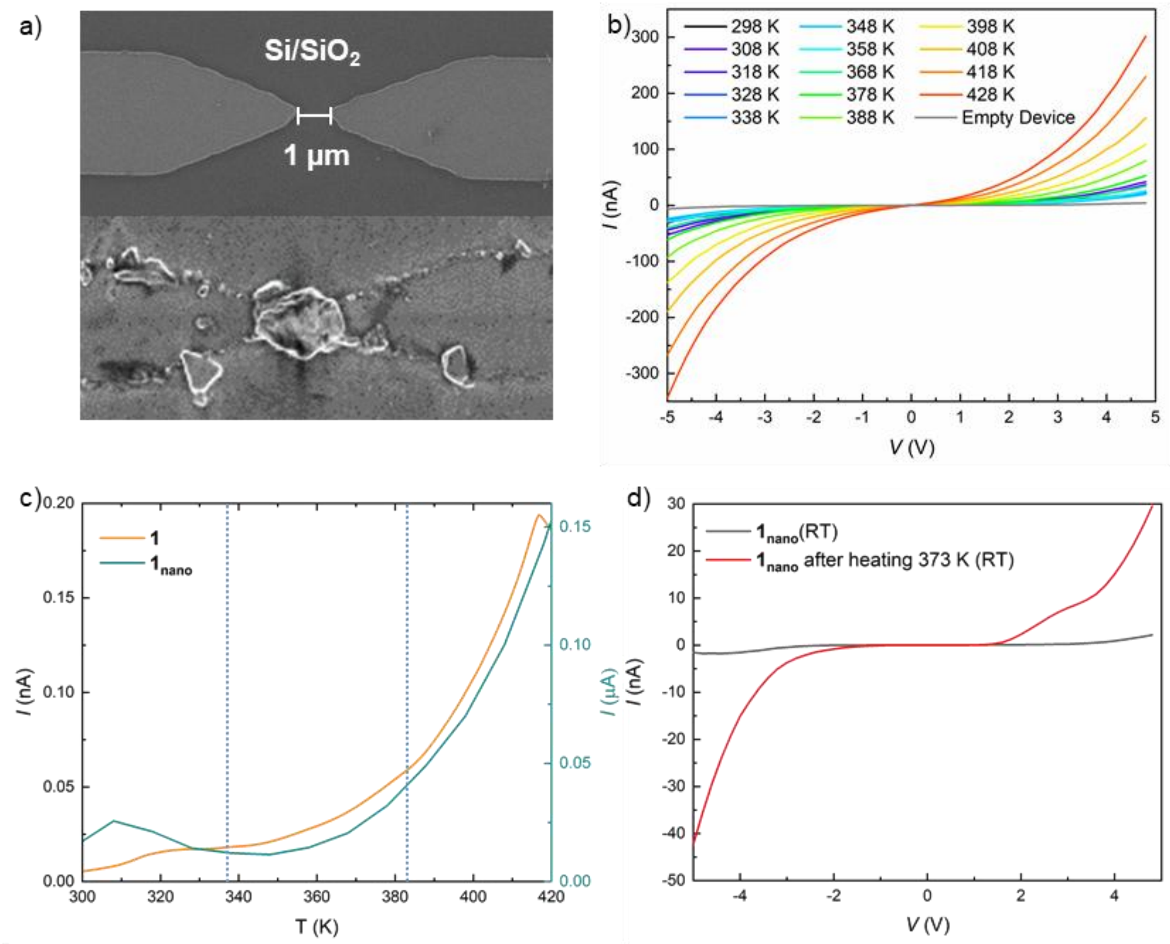

Figure 5. a) SEM image of a representative finger-like electrode device before (top) and after dielectrophoresis (bottom). b) Current–Voltage (*IV*) characteristics of $\mathbf{1}_{\mathbf{nano}}$ measured at different temperatures. c) *I* measured as a function of T at a fixed $V = 4$ V (blue dotted lines show the structural transformations of **1**[44]). d) *IV* characteristics measured at room temperature of $\mathbf{1}_{\mathbf{nano}}$ before and after heating up to 373 K.

The initial decrease of current with temperature in $\mathbf{1}_{\mathbf{nano}}$, consistently observed in different nanocrystals (**Figure S14-S16**), is not observed in **1**. This different behavior for the low temperature region may be indicative of a different relaxation process at low temperatures or different water dynamics when downsizing the material to the nanoscale.

Finally, to check whether the increase in current was simply due to the temperature or, as in the case of **1**, to the new configuration in which all the metal centers are in LS and therefore, in the highest conducting configuration for this system, the experiment shown in **Figure 5d** was carried out. The current was measured in a device, after trapping $\mathbf{1}_{\mathbf{nano}}$ by DEP, at room temperature (black plot). Afterwards, the same device was heated up to 373 K and kept at that temperature for 20 minutes and then cooled down to room temperature again to measure the current (red plot). The results show that at the same temperature, the current obtained when $\mathbf{1_{nano}}$ is in a configuration with a higher percentage of LS metal centers is up to one order of magnitude higher.

2.5. Conclusion

Here, a robust 3D SCO MOF, $[Fe_2(H_{0.67}bdt)_3]\cdot xH_2O$ (**1**), has been subjected to a sonication-assisted downsizing process, resulting in nanocrystals ($\mathbf{1_{nano}}$) from the as-synthetized macrocrystals (**1**). Multiscale materials characterization confirmed this transformation, with MicroED revealing the preservation of the crystalline structure in $\mathbf{1_{nano}}$. Raman spectroscopy demonstrated that the size reduction has not affected the SCO behavior. Indeed, $\mathbf{1_{nano}}$ is capable of releasing water molecules located in the pores, triggering a reverse HS to LS transition. This transition is accompanied by a dynamic structural adaptation of the framework, involving phenyl rotation and changes in ligand binding. These changes are evidenced by shifts in the $\nu_{Fe\text{-}N}$ and ν_{rings} bands observed in the Raman spectra.

Ultimately, this also results in the preservation of the electrical properties, which have been shown to be similar to those of its bulk counterpart. *IV* measurements were conducted on nanofabricated devices with $\mathbf{1_{nano}}$ deposited *via* dielectrophoresis in the gaps between gold electrodes. As in **1**, a current increase of one order of magnitude was obtained for $\mathbf{1_{nano}}$ as a function of water release-triggered HS to LS switch. All in all, this innovative nanostructuring technique for 3D materials paves the way for their technological exploitation in nanodevices while preserving their original properties. In addition, MicroED proves to be a powerful tool for characterizing nanocrystal structures.

2.6. Experimental Section/Methods

Obtention of $\mathbf{1_{nano}}$

To obtain $\mathbf{1_{nano}}$, 1 mg of **1** was suspended in 1 mL of isopropanol and subjected to ultrasound irradiation at a power of 280 W for 20 minutes. Sonication serves several critical functions in this process. Firstly, it provides the energy necessary to break down larger crystals into smaller nanocrystals through the generation of cavitation bubbles that collapse violently, creating intense localized forces.[58] This mechanical agitation helps in dispersing the particles uniformly within the solvent, preventing aggregation. Additionally, sonication enhances the solvent penetration into the crystal lattice, facilitating more effective and uniform fragmentation.[58] Following sonication, the suspension underwent centrifugation (3000 rpm, 15 minutes, RT) to separate the larger crystals, retaining the nanocrystals in the supernatant (**Figure S1†**).

Materials and methods

All reagents and solvents were commercially available and used as received. The $FeSO_4 \cdot 7H_2O$ was purchased from Scharlab while the precursors of the H_2bdt ligand (1,4-dicyanobenzene, sodium azide and pyridinium hydrochloride) and the NaSCN were purchased from Merck. The H_2bdt ligand and **1** were synthesized using a method reported in the literature[45,46] with modifications.[44]

For MicroED analyses, Quantifoil Cu 300 R2/2 pitted carbon grids were glow discharged at 25 mA for 30" immediately prior to sample addition. A volume of 3 μL of the crystalline solution was added to each prepared grid, blotted manually on the back with WhatmanTM ashless filter papers, and immediately vitrified manually in liquid ethane.

The grids were loaded onto a Thermo ScientificTM TalosTM ArcticaTM transmission electron microscope (200 kV) equipped with a Ceta-D detector for analysis at 100 K and a wavelength of 0.025082 Å. A manual search for diffracting crystals along the grating was conducted. Subsequently, the most suitable crystals were selected for Electron Diffraction collection collected using the EPUD software (version 1.17.0.6389). They were collected using a stage tilt of 100° (with 1° increments) and an exposure time per frame of 0.5 seconds, resulting in a total dose applied to each crystal of 1.97 e/A2s. The data was initially processed and scaled using the XDSGUI package[59] for later structure resolution and refinement.

Electron diffraction data for **1nano** were treated with APEX4 software. Saint was used for integration. The structures were solved by intrinsic phasing methods using SHELXT[60] and refined on F2. Hydrogen atoms were included at the calculated positions, riding on their carrier atoms at neutron diffraction data distances. Data refinement was performed in OLEX and ShelXle[61] softwares using SHELXL, including specific dispersion factors for the wavelength and atomic scattering factors for electrons.

Raman spectra were acquired with a Bruker Senterra confocal Raman microscope (Bruker Optic, Ettlingen, Germany, resolution 3–5 cm^{-1}) system. The excitation was carried out using a 532 nm laser excitation beam, with a 20× or 100× objective for **1** and **1nano**, respectively, 0.02 mW maximum power, 2 s acquisition time and 4 repetitions. The reported Raman spectra are the result of the average over at least 3 points on a single crystal of **1** or nanocrystals of **1nano** drop-casted on filter paper. In the case of the study conducted on **1** after dielectrophoresis for their deposition in the channels between gold electrodes, the reported Raman spectra are the result of the average over 21 points collected among at least 3 different electrodic channels. In the case of Raman spectroscopy on dehydrated samples, spectra were collected after a thermal treatment at 373 K for 30 min. Temperature dependent Raman spectroscopy on **1** single crystals and **1nano** drop-casted on the electrical devices in a Linkam T95 system with a LNP 95 Liquid Nitrogen Cooling System, in N_2 atmosphere, with a 2K/min heating rate and Raman spectra were collected every 10K, after equilibration for 5 min, with a 50× long working distance objective, 0.02 mW maximum power, 2 s acquisition time and 4 repetitions. The reported Raman spectra are the result of the average over at least 3 points.

AFM images are acquired using commercial AFM systems (NT-MDT Ntegra Prima and JPK Nanowizard 2) in semicontact (dynamic) mode in ambient conditions. NSC14/Cr-Au BS silicon cantilevers, with typical values of 5.0 $N \cdot m^{-1}$ spring constant and 160 kHz resonant frequency are employed in all cases. The resulting images are processed using WSxM software[62] (version 5.0, Nanotec Electronica S.L., Tres Cantos, Spain) and the statistical analysis is done using Gwyddion software. Scanning Electron Microscopy (SEM) images were obtained in a field emission (FE-SEM), SIGMA 360 VP Carl Zeiss equipment, at 2kV (vacuum level 10^{-10} mbar). DC electron transport measurements were carried out on devices where $\mathbf{1_{nano}}$ is deposited *via* dielectrophoresis (DEP) using a Keithley 2450 SourceMeter under light. The temperature was controlled using a Linkam T95 system with a LNP 95 Liquid Nitrogen Cooling System, with a heating rate of 2 K min^{-1} in the range 298-428 K. After reaching the desired temperature an equilibration time of 10 min preceded the measurements.

Device fabrication: arrays of 5 nm Cr/80 nm Au electrodes spaced 1 μm apart are produced on a Si/SiO_2 substrate using maskless laser lithography followed by metal evaporation. Each electrode has a width of 4 μm and is connected to a 2.5 mm x 2.5 mm contact pad. The devices were fabricated via maskless laser optical lithography. The electrodes are deposited on highly-doped silicon (Si) wafers capped with a 300 nm thick insulating SiO_2 layer.

Dielectrophoresis(DEP) trapping of the nanocrystals is performed using a FeelTech FY3200S Dual-channel Arbitrary Function Signal Generator, applying the following parameters: V_{AC} = 10 V, ν = 1 MHz, and t = 3 min.

[CCDC 2384435 and 2385242 contains the supplementary crystallographic data for this paper. These data can be obtained free of charge from The Cambridge Crystallographic Data Centre via www.ccdc.cam.ac.uk/data_request/cif.]

Supporting Information

Supporting Information is available from the Wiley Online Library or from the author.

Acknowledgements

JSC thanks funds from the Spanish MICINN through National Research Project (PID2022-141738NB-I00 and TED2021-131018B-C22) and the MAD2D-CMMRR MATERIALES AVANZADOS-IMDEANC-4. AM-M thanks funds from the Spanish MICINN through PRE2019-C-87849. IMDEA Nanociencia acknowledges support from the ‘Severo Ochoa’ Programme for Centres of Excellence in R&D (MINECO, Grant CEX2020-001039-S). This work has received support from grants RYC2019-028429-I (EB), TED2021-130957B-C55 (EB) and PID2022-140923NB-C22 funded by MCIN/AEI/10.13039/501100011033. The authors acknowledge the Center for Micro and Nanofabrication at IMDEA Nanociencia for the device fabrication. We thank the XALOC-ALBA synchrotron source under project 2023017235.

References

[1] H. Furukawa, K. E. Cordova, M. O'Keeffe, O. M. Yaghi, *Science* **2013**, *341*, 1230444.

[2] H. Wang, Q.-L. Zhu, R. Zou, Q. Xu, *Chem* **2017**, *2*, 52.

[3] S. Kuyuldar, D. T. Genna, C. Burda, *J. Mater. Chem. A* **2019**, *7*, 21545.

[4] K. Senthil Kumar, M. Ruben, *Coord. Chem. Rev.* **2017**, *346*, 176.

[5] G. Molnár, S. Rat, L. Salmon, W. Nicolazzi, A. Bousseksou, *Adv. Mater.* **2018**, *30*, 1703862.

[6] E. Coronado, *Nat. Rev. Mater.* **2020**, *5*, 87.

[7] J. Wang, I. Imaz, D. Maspoch, *Small Struct.* **2022**, *3*, 2100126.

[8] A. Enríquez-Cabrera, K. Ridier, L. Salmon, L. Routaboul, A. Bousseksou, *Eur. J. Inorg. Chem.* **2021**, 2000.

[9] C. Bartual-Murgui, A. Akou, C. Thibault, G. Molnár, C. Vieu, L. Salmon, A. Bousseksou, *J. Mater. Chem. C* **2015**, *3*, 1277.

[10] E. Resines-Urien, L. Piñeiro-López, E. Fernandez-Bartolome, A. Gamonal, M. Garcia-Hernandez, J. Sanchez Costa, *Dalton Trans.* **2020**, *49*, 7315.

[11] O. Kahn, C. J. Martinez, *Science* **1998**, *279*, 44.

[12] J. Larionova, L. Salmon, Y. Guari, A. Tokarev, K. Molvinger, G. Molnár, A. Bousseksou, *Angew. Chem. Int. Ed.* **2008**, *47*, 8236.

[13] E. Resines-Urien, M. Á. G. García-Tuñón, M. García-Hernández, J. A. Rodríguez-Velamazán, A. Espinosa, J. S. Costa, *Advanced Science* **2022**, *9*, 2202253.

[14] E. Resines-Urien, E. Fernandez-Bartolome, A. Martinez-Martinez, A. Gamonal, L. Piñeiro-López, J. Sanchez Costa, *Chem. Soc. Rev.* **2023**, *52*, 705.

[15] C. Lefter, S. Rat, J. Sanchez Costa, M. D. Manrique-Juárez, C. M. Quintero, L. Salmon, I. Séguy, T. Leichle, L. Nicu, P. Demont, A. Rotaru, G. Molnár, A. Bousseksou, *Adv. Mater.* **2016**, *28*, 7508.

[16] C. Gobel, C. Hils, M. Dreschler, D. Baabe, A. Greiner, H. Schmalz, B. Weber, *Angew. Chem. Int. Ed.* **2020**, *59*, 5765.

[17] G. A. Craig, J. Sanchez Costa, O. Roubeau, S. J. Teat, G. Aromí, *Chem. Eur. J.* **2011**, *17*, 3120.

[18] A. Martinez-Martinez, P. Albacete, M. García-Hernández, E. Resines-Urien, D. Fairen-Jimenez, J. Sánchez Costa, *Dalton Trans.* **2024**, *53*, 9257.

[19] N. A. A. M. Amin, S. M. Said, M. F. M. Salleh, A. M. Afifi, N. M. J. N. Ibrahim, M. M. I. M. Hasnan, M. Tahir, N. Z. I. Hashim, *Inorganica Chim. Acta* **2023**, *544*, 121168.

[20] V. Rubio-Giménez, S. Tatay, C. Martí-Gastaldo, *Chem. Soc. Rev.* **2020**, *49*, 5601.

[21] Y. Hu, X. Dong, J. Nan, W. Jin, X. Ren, N. Xu, Y. M. Lee, *Chem. Commun.* **2011**, *47*, 737.

[22] D. Zacher, A. Baunemann, S. Hermes, R. A. Fischer, *J. Mater. Chem.* **2007**, *17*, 2785.

[23] C.-W. Kung, T.-H. Chang, L.-Y. Chou, J. T. Hupp, O. K. Farha, K.-C. Ho, *Chem. Commun.* **2015**, *51*, 2414.

[24] B. D. Dhanapala, D. L. Maglich, M. E. Anderson, *Langmuir* **2023**, *39*, 12196.

[25] Z. Wang, C. Wöll, *Adv. Mater. Technol.* **2019**, *4*, 1800413.

[26] P. Horcajada, C. Serre, D. Grosso, C. Boissière, S. Perruchas, C. Sanchez, G. Férey, *Advanced Materials* **2009**, *21*, 1931.

[27] A. Demessence, P. Horcajada, C. Serre, C. Boissière, D. Grosso, C. Sanchez, G. Férey, *Chem. Commun.* **2009**, 7149.

[28] A. Demessence, C. Boissière, D. Grosso, P. Horcajada, C. Serre, G. Férey, G. J. A. A. Soler-Illia, C. Sanchez, *J. Mater. Chem.* **2010**, *20*, 7676.

[29] P. Amo-Ochoa, L. Welte, R. González-Prieto, P. J. Sanz Miguel, C. J. Gómez-García, E. Mateo-Martí, S. Delgado, J. Gómez-Herrero, F. Zamora, *Chem. Commun.* **2010**, *46*, 3262.

[30] A. Abbasi, T. Moradpour, K. Van Hecke, *Inorganica Chimica Acta* **2015**, *430*, 261.
[31] P.-Z. Li, Y. Maeda, Q. Xu, *Chem. Commun.* **2011**, *47*, 8436.
[32] H. Kaur, J. N. Coleman, *Adv. Mater.* **2022**, *34*, 2202164.
[33] C. L. Ruiz-Zambrana, M. Malankowska, J. Coronas, *Dalton Trans.* **2020**, *49*, 15139.
[34] E. A. Flügel, A. Ranft, F. Haase, B. V. Lotsch, *J. Mater. Chem.* **2012**, *22*, 10119.
[35] L. Meng, B. Yu, Y. Qin, *Commun. Chem.* **2021**, *4*, 82.
[36] M. Zhao, Y. Huang, Y. Peng, Z. Huang, Q. Ma, H. Zhang, *Chem. Soc. Rev.* **2018**, *47*, 6267.
[37] Z. Huang, M. Ge, F. Carraro, C. Doonan, P. Falcaro, X. Zou, *Faraday Discuss.* **2021**, *225*, 118.
[38] C. Ma, C. Lin, J. Li, *Chin. J. Struct. Chem.* **2023**, 100209.
[39] H. Mba, M. Picher, N. Daro, M. Marchivie, P. Guionneau, G. Chastanet, F. Banhart, *J. Phys. Chem. Lett.* **2023**, *14*, 8100.
[40] X. Mu, C. Gillman, C. Nguyen, T. Gonen, *Annu. Rev. Biochem.* **2021**, *90*, 431.
[41] A. A. Bardin, A. Haymaker, F. Banihashemi, J. Y. S. Lin, M. W. Martynowycz, B. L. Nannenga, *Ultramicroscopy* **2024**, *257*, 113905.
[42] B. Wang, T. Rhauderwiek, A. K. Inge, H. Xu, T. Yang, Z. Huang, N. Stock, X. Zou, *Chem. Eur. J.* **2018**, *24*, 17429.
[43] D. Denysenko, M. Grzywa, M. Tonigold, B. Streppel, I. Krkljus, M. Hirscher, E. Mugnaioli, U. Kolb, J. Hanss, D. Volkmer, *Chem. Eur. J.* **2011**, *17*, 1837.
[44] A. Martinez-Martinez, E. Resines-Urien, L. Piñeiro-López, A. Fernández-Blanco, A. Lorenzo Mariano, J. Albalad, D. Maspoch, R. Poloni, J. A. Rodríguez-Velamazán, E. C. Sañudo, E. Burzurí, J. Sanchez Costa, *Chem. Mater.* **2023**, *35*, 6012.
[45] Z. Yan, M. Li, H.-L. Gao, X.-C. Huang, D. Li, *Chem. Commun.* **2012**, *48*, 3960.
[46] W.-T. Liu, J.-Y. Li, Z.-P. Ni, X. Bao, Y.-C. Ou, J.-D. Leng, J.-L. Liu, M.-L. Tong, *Cryst. Growth Des.* **2012**, *12*, 1482.
[47] R. Quirós-Ovies, M. Laborda, N. M. Sabanés, L. Martín-Pérez, S. M.-D. Silva, E. Burzurí, V. Sebastian, E. M. Pérez, J. Santamaría, *ACS Nano* **2023**, *17*, 5984.
[48] L. Martín-Pérez, S. Medina Rivero, M. Vázquez Sulleiro, A. Naranjo, I. J. Gómez, M. L. Ruíz-González, A. Castellanos-Gomez, M. Garcia-Hernandez, E. M. Pérez, E. Burzurí, *ACS Nano* **2023**, *17*, 3007.
[49] L. Martín-Pérez, E. Burzurí, *Molecules* **2021**, *26*, 7371.
[50] S. Roy, Z. Huang, A. Bhunia, A. Castner, A. K. Gupta, X. Zou, S. Ott, *J. Am. Chem. Soc.* **2019**, *141*, 15942.
[51] Q. Chen, G. Zhou, Z. Huang, *Acc. Chem. Res.* **2024**, *57*, 2522.
[52] G. A. Craig, J. Sanchez Costa, O. Roubeau, S. J. Teat, H. J. Shepherd, M. Lopes, G. Molnár, A. Bousseksou, G. Aromí, *Dalton Trans.* **2014**, *43*, 729.
[53] G. Brehm, M. Reiher, B. Le Guennic, L. Leibold, S. Schindler, F. W. Heinemann, S. Schneider, *J. Raman Spectrosc.* **2006**, *37*, 108.
[54] Z. G. Lada, *Magnetochemistry* **2022**, *8*, 108.
[55] A. Bousseksou, J. J. McGarvey, F. Varret, J. A. Real, J.-P. Tuchagues, A. C. Dennis, M. L. Boillot, *Chem. Phys. Lett.* **2000**, *318*, 409.
[56] F. Kobayashi, Y. Komatsumaru, R. Akiyoshi, M. Nakamura, Y. Zhang, L. F. Lindoy, S. Hayami, *Inorg. Chem.* **2020**, *59*, 16843.
[57] T. P. Gerasimova, S. A. Katsyuba, L. G. Lavrenova, V. Pelmenschikov, M. Kaupp, *J. Mol. Struct.* **2015**, *1101*, 8.
[58] C. Vaitsis, G. Sourkouni, C. Argirusis, *Ultrason. Sonochem.* **2019**, *52*, 106.
[59] W. Brehm, J. Triviño, J. M. Krahn, I. Usón, K. Diederichs, *J. Appl. Crystallogr.* **2023**, *56*, 1585.
[60] G. M. Sheldrick, *Acta Crystallogr. A Found Adv.* **2015**, *71*, 3.
[61] C. B. Hübschle, G. M. Sheldrick, B. Dittrich, *J. Appl. Crystallogr.* **2011**, *44*, 1281.

[62] I. Horcas, R. Fernández, J. M. Gómez-Rodríguez, J. Colchero, J. Gómez-Herrero, A. M. Baro, *Rev. Sci. Instrum* **2007**, *78*, 013705.